The Astrophysical Journal Letters, 985:L23 (10pp), 2025 May 20 https://doi.org/10.3847/2041-8213/add470

The Striated Solar Photosphere Observed at 0.″03 Resolution

David Kuridze[1], Friedrich Wöger[1], Han Uitenbroek[1], Matthias Rempel[2], Alexandra Tritschler[1], Thomas Rimmele[1], Catherine Fischer[1,3], and Oskar Steiner[4,5]
[1] National Solar Observatory, 3665 Discovery Drive, Boulder, CO 80303, USA; dkuridze@nso.edu
[2] High Altitude Observatory, NSF National Center for Atmospheric Research, Boulder, CO 80307, USA
[3] European Space Agency (ESA), European Space Astronomy Centre (ESAC), Camino Bajo del Castillo s/n, 28692 Villanueva de la Cañada, Madrid, Spain
[4] Kiepenheuer-Institut für Sonnenphysik (KIS), Georges-Köhler-Allee 401a, 79110 Freiburg, Germany
[5] Istituto ricerche solari Aldo e Cele Daccó (IRSOL), Via Patocchi 57, 6605 Locarno-Monti, Switzerland
Received 2025 April 4; revised 2025 April 29; accepted 2025 May 6; published 2025 May 20

Abstract

Striated granular edges observed in the solar photosphere represent one of the smallest-scale phenomena on the Sun. They arise from the interaction of strongly coupled hydrodynamic, magnetic, and radiative properties of the plasma. In particular, modulations in the photospheric magnetic field strength cause variations in density and opacity along the line of sight, leading to their formation. Therefore, the striation patterns can be used as valuable diagnostics for studying the finest-scale structure of the photospheric magnetic field. The Daniel K. Inouye Solar Telescope (DKIST) allows observations of the solar atmosphere with a spatial resolution of better than 0.″03 with its current instrumentation. We analyze images acquired with the Visible Broadband Imager using the *G*-band channel to investigate the characteristics of fine-scale striations in the photosphere and compare them with state-of-the-art radiation-MHD simulations at similar spatial resolution. Both observed and synthetic images reveal photospheric striae with widths of approximately 20−50 km, suggesting that at least 4 m class solar telescopes are necessary to resolve this ultrafine structure. Analysis of the numerical simulations confirms that the striation observed in the filtergrams is associated with spatial variations in photospheric magnetic flux concentrations, which cause shifts in the geometrical height where the emergent intensity forms. Some fine-scale striations in the synthetic images originate from magnetic field variations of approximately 100 G, resulting in Wilson depressions as narrow as 10 km. This suggests that DKIST *G*-band images can trace the footprints of magnetic field variations and Wilson depressions at a similar scale.

Unified Astronomy Thesaurus concepts: Ground-based astronomy (686); Ground telescopes (687); Solar photosphere (1518); Radiative transfer (1335); Magnetohydrodynamical simulations (1966)

1. Introduction

Fine-scale striation in the solar photosphere is commonly observed in features known as faculae—bright granular edges that appear in active region plages when viewed away from the disk center (DC; H. C. Spruit 1976; T. E. Berger et al. 1995; T. E. Berger & A. M. Title 2001; J. Hirzberger & E. Wiehr 2005). Another characteristic of faculae is the presence of a prominent dark lane on the DC side of the bright granular edge.

A series of excellent studies dedicated to the theoretical and observational aspects of faculae was published between 2004 and 2005 (T. E. Berger et al. 2004; M. Carlsson et al. 2004; C. U. Keller et al. 2004; B. W. Lites et al. 2004; O. Steiner 2005). The center-to-limb variation of *G*-band images synthesized from advanced radiative magnetoconvective simulations closely reproduces the main observational characteristics of the plage-type photosphere, including faculae. In particular, similar to observations, magnetic flux concentrations (MFCs) appear bright and with enhanced contrast in *G*-band images at or near the DC (R. J. Rutten et al. 2001; O. Steiner et al. 2001; M. Schüssler et al. 2003). This occurs due to the low-density, low-opacity environment along the flux tube, which results in a depression of the optical-depth unity surface where the plasma temperature is higher than outside the flux tube at the same optical depth. Toward the limb, when MFCs are viewed at an angle, only a portion of the vertically oriented magnetic flux tubes intersects the line of sight (LoS), leading to the formation of facular brightenings and dark lanes (M. Carlsson et al. 2004; C. U. Keller et al. 2004; O. Steiner 2005).

The first detection of striation in photospheric faculae was made with ∼0.″1 resolution observations using 1 m-class solar telescopes. First, thin, dark stripes in faculae were seen in the data obtained from the Swedish Solar Telescope (SST) using blue-continuum filtergrams centered at 487.7 nm (B. W. Lites et al. 2004). Later, M. Carlsson et al. (2004), B. De Pontieu et al. (2006), and T. E. Berger et al. (2007) also detected adjacent, thin, dark striations extending along faculae in the limbward direction, using *G*-band images from the SST.

B. De Pontieu et al. (2006) studied the temporal evolution of facular elements and concluded that the striation is a highly dynamic phenomenon characterized by merging, splitting, and rapid motions on timescales of the order of minutes.

It has been proposed that the striation is generated by spatial variations in the magnetic field strength along the LoS in front of faculae (M. Carlsson et al. 2004; B. De Pontieu et al. 2006). Individual dark stripes are associated with weak MFCs, while the bright space in between is due to strong magnetic fields, which act as radiative channels due to their material deficiency and increased transparency. T. E. Berger et al. (2007) showed that the striation in *G*-band images is closely correlated with the variation in the magnetic flux density measured in simultaneous

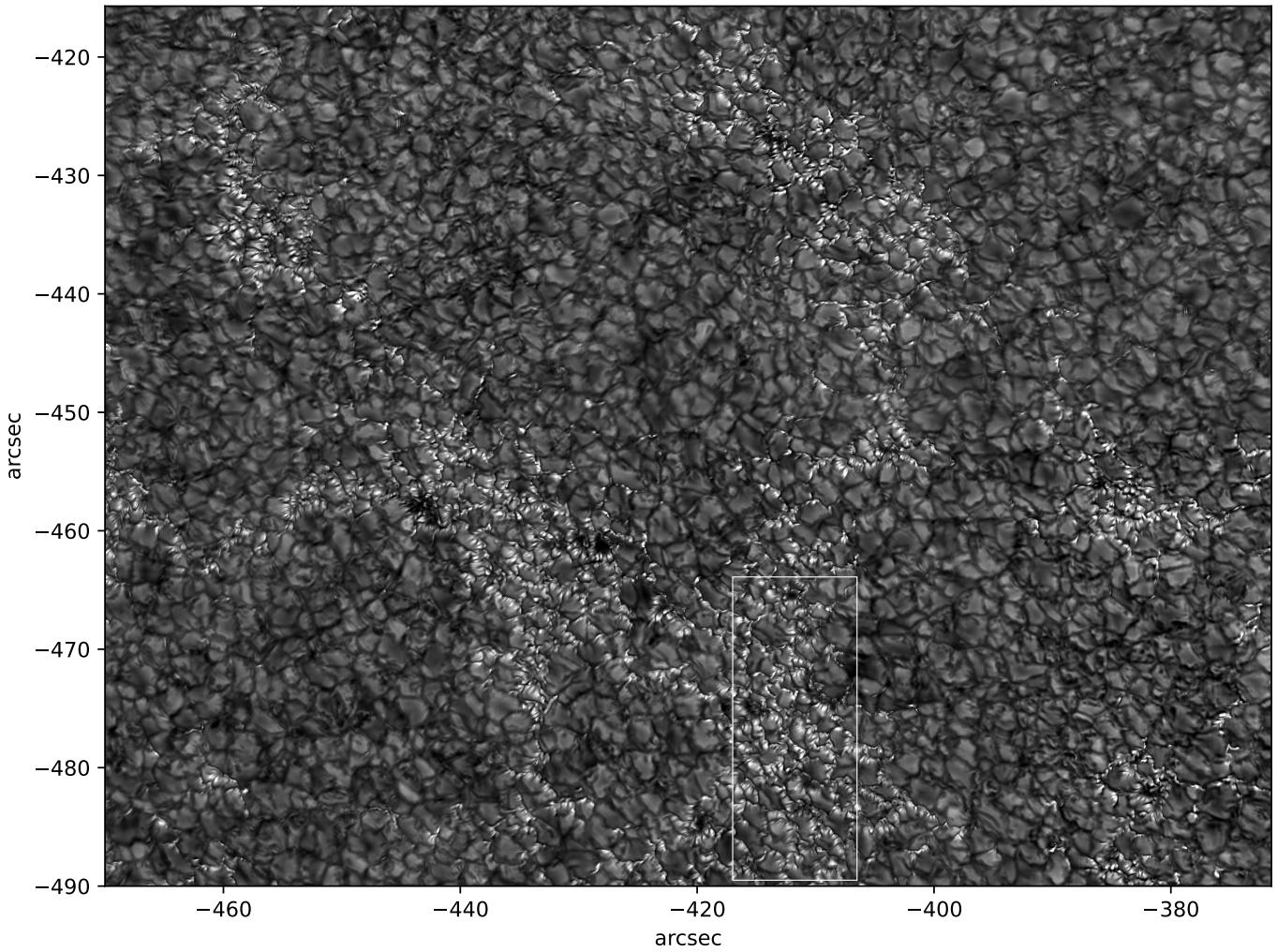

Figure 1. Mosaic of high-resolution *G*-band filtergrams obtained with the VBI instrument on 2022 June 3 at 17:46 UT. The white box indicates the plage region shown in Figure 2.

photospheric magnetograms. Therefore, striation provides a unique opportunity to observe and investigate the small-scale structure and spatiotemporal variation of MFCs. Moreover, its dynamics offer the possibility to directly peer at the source of mechanical energy at the basis of MFCs in the photosphere. The width of individual striae has been estimated to be at or below the resolution limits of 1 m-class solar telescopes. Based on SST data, the average width of the individual strands is around 0.″1–0.″2, which is indeed close to the diffraction limit of SST (B. W. Lites et al. 2004; B. De Pontieu et al. 2006; T. E. Berger et al. 2007).

In this work, we investigate the photospheric striation for the first time with a spatial resolution of 0.″03, using Daniel K. Inouye Solar Telescope Visible Broadband Imager (DKIST/VBI) data (F. Wöger et al. 2021). We reproduce our observations using an advanced 3D MHD simulation at a comparable resolution, combined with spectral line synthesis, to examine the formation of the striation on faculae and its connection with photospheric magnetic field variations.

2. Observations

The observations used in this Letter were obtained between 17:09 and 19:20 UT on 2022 June 3 with the VBI (F. Wöger et al. 2021) deployed at DKIST (T. R. Rimmele et al. 2020). The heliocentric coordinates of the center of the field of view (FOV) covered by the observations were $(x, y) = (-420'', -450'')$, with heliocentric angle $\mu \approx 0.85$ (see Figure 1).

We used the VBI blue branch to obtain filtergrams, sequentially in *G* band, Ca II K, and Hβ, using interference filters mounted on a rotating filterwheel. The *G*-band filter is centered at 430.52 nm with an FWHM of approximately 0.437 nm. The instantaneous FOV of the VBI blue is $45'' \times 45''$ with a spatial sampling of 0.″011 pixel^{-1}. For these observations, we employed the so-called "field-sampling mode" to cover the full DKIST FOV of $2' \times 2'$ with a mosaic of 3×3 tiles. All VBI images were reconstructed using the speckle code of F. Wöger et al. (2008) to remove residual atmospheric distortion from the data, bringing the effective time step to 3 s per tile. Hence, for any given filter channel, the full DKIST FOV was sampled in 27 s, and the overall cadence for the three filters was 81 s. More details on the observations and data can be found in D. Kuridze et al. (2024).

Seeing conditions during the approximately 2 hr of observation varied but were on average good throughout the observations. Following reconstruction, we estimate that multiple frames achieved a spatial resolution close to the diffraction limit (0.″022–0.″03 at 430 nm) based on the size of the smallest resolved structures observed in the data.

3. Numerical Simulations and Spectral Synthesis

3.1. Simulations

We carried out numerical simulations using the radiative MHD code MURaM (M. Rempel 2014). We use a setup representative of an enhanced magnetic network region with a mean net vertical magnetic flux density of 200 G, which is based on models presented in M. Rempel (2020) and K. L. Yeo et al. (2020). The absolute (unsigned) mean magnetic flux density is 260 G at $\tau_{500\,\mathrm{nm}} = 1$ due to the presence of a small-scale dynamo. The numerical domain has an extent of $9 \times 9 \times 3.24\,\mathrm{Mm}^3$ (top panels of Figure 3); the vertical extent covers about 2.24 Mm of the convection zone below the base of the photosphere ($\tau_{500\,\mathrm{nm}} = 1$) and 1 Mm of the solar atmosphere above $\tau_{500\,\mathrm{nm}} = 1$. The side boundaries are periodic, the bottom boundary is open for convective flows, and the top boundary is open for upflows, while downflows are suppressed. The magnetic bottom boundary condition allows for the transport of the horizontal magnetic field (see M. Rempel 2014 for details) and the top boundary imposes a potential field. The original simulation in M. Rempel (2020) and K. L. Yeo et al. (2020) started from a small-scale dynamo setup with an added uniform vertical magnetic field of 200 G and was evolved for 18 hr. We continued the simulation for 4000 s and then regridded to our final grid spacing of 7.03125 km in the horizontal x- and y-directions and 5 km in the vertical z-direction. The simulation ran for another 1000 s at this resolution with 5 s cadence. To capture the center-to-limb variation effects more accurately, the photospheric abundances of M. Asplund et al. (2009) and 12-band opacity were used in the simulation.

3.2. Radiative Transfer

One of the developed snapshots of the simulation was used to generate the synthetic G-band spectrum for a wavelength interval between 429 and 432 nm, using 3000 spectral points with the 1D version of the radiative transfer code Rybicki–Hummer (RH; H. Uitenbroek 2001) in local thermodynamic equilibrium. Intensities were also synthesized at a single continuum wavelength of 500 nm. To save computational time the vertical grid space was reduced to 10 km by using only every second grid point along the vertical axes. We synthesized spectra at the disk and toward the limb at $\mu = 1$ and 0.85, respectively, where μ is the cosine of heliocentric angle, θ (middle row of Figure 3).

To synthesize G-band intensities at $\mu = 0.85$, the MURaM cube was modified by shifting each horizontal layer relative to the layer below by $\Delta z \tan\theta$, where Δz represents the vertical grid spacing. This adjustment aligns the slanted LoS direction vertically. Pixel sampling was foreshortened along the y-direction by a factor of $\sqrt{1-\mu^2}$ and increased along the z-direction by a factor of $1/\mu$ for the $\mu = 0.85$ data.

To closely replicate the DKIST G-band filtergrams, the synthetic data were multiplied by the VBI transmission profile (bottom panel of Figure 3) and integrated over the whole wavelength range covered by the VBI filter. To investigate the polarization signatures of the intensity striation, we also synthesized the full Stokes profiles of the magnetically sensitive Fe I 630.2 nm photospheric line, using the same MURaM cube at $\mu = 0.85$.

4. Analysis and Results

4.1. DKIST Filtergrams

Figure 1 displays the G-band image of the plage region taken on 2022 June 3 at 18:36 UT. The plage is dominated by facular brightenings that are associated with strong MFCs (see Figures 1 and 2 in D. Kuridze et al. 2024). The zoomed G-band image in the left panel of Figure 2 shows all facular features, such as bright granular edges that are bordered by dark lanes on the DC side. The bright granular edges are dominated by a pattern of striations—fine-scale, short, dark features that are mostly parallel to each other and extended toward the limb (Figure 2).

To enhance the fine-scale details and structure of the striation, we applied a Gaussian-filter subtraction method to the images. In particular, images are blurred with two different Gaussian kernels (with $\sigma = 1$ and 3) and subtracted from each other. The resulting image is displayed in the right panel of Figure 2. It shows that all facular brightenings are striated with very thin and short features.

To quantify the width of the striae, we measured the FWHM of the Gaussian fits to the intensity profiles along crosscuts of individual striae. Figure 4 shows the intensity profiles of eight randomly selected dark striae, along with their Gaussian fits. The FWHM of these profiles ranges from 20 to 53 km. The classical theoretical resolution limit ($1.22\lambda/D$) for DKIST/G band is $\sim$20 km.

4.2. Synthetic Data

Figure 3, middle row of panels, presents synthetic G-band images for heliocentric angles $\mu = 1$ (left panel, DC) and $\mu = 85$ (right panel, off DC), whereby the spectrally resolved G-band spectrum was multiplied with the VBI transmission profile and integrated over the wavelength range covered by the filter. All common G-band features seen in the observations are reproduced in the simulated images, including magnetic bright points at DC and striated bright faculae and dark lanes at $\mu = 85$. The bottom panel shows in blue the spectrally resolved G-band spectrum averaged over the full FOV of the simulation, together and overplotted with the Fourier transform spectrometer (FTS) solar spectrum (H. Neckel & D. Labs 1984) of the same wavelength range (orange). They agree with each other to a high level of detail. The very good agreement of synthetic and observational data in terms of facular details and the G-band spectrum suggests that the simulated data can serve as a powerful diagnostics of G-band intensities.

4.3. Dark Lanes and Facular Brightenings

From the MURaM snapshot, we also calculated the height of the surface where the optical depth reaches unity at different wavelength positions along the G band. The top panels of Figure 5 present a small FOV of the full synthetic G-band image and the corresponding map of the height where the optical depth is unity in the G-band continuum at 430.7 nm (hereafter referred to as $\tau = 1$) for the heliocentric angle $\mu = 0.85$. The map reveals that the formation heights of the $\tau = 1$ surface in the dark lanes and bordering granules on the DC side are very similar (top row of Figure 5). However, the areas next to dark lanes on the limb side, where facular brightenings appear in the G-band images, show the $\tau = 1$

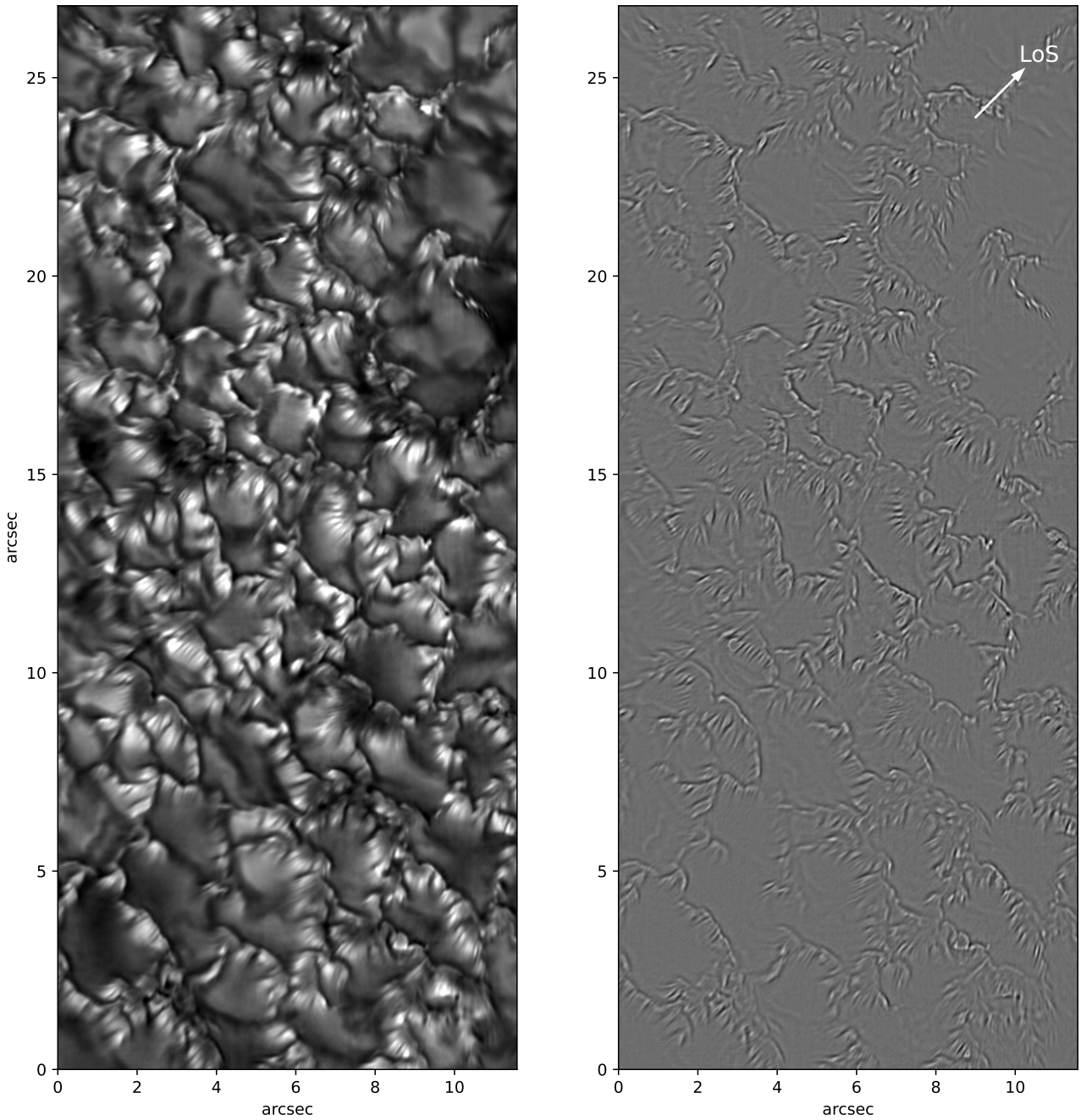

Figure 2. Left: zoomed image of the *G*-band facular region indicated by the white box in Figure 1. Right: the same image processed with a Gaussian-filter subtraction method (see text for an explanation). The direction arrow points in the direction of the DC.

surface to lie deeper compared to other parts of the granules and the dark lanes (top panels of Figure 5).

The bottom panels of Figure 5 display the vertical cuts through the temperature and LoS magnetic field strength along the blue dotted lines marked in the top panels. Isothermal contours at $T = 6000$ and 7000 K are overplotted in white. Blue lines follow the $\tau = 1$ height. The base of the photosphere (the zero-point of the geometrical height scale, $z = 0$) is defined as the average height where optical depth at 500 nm is unity at DC. The diagrams in the bottom panels of Figure 5 confirm that the continuum intensity from the dark lane forms in a very similar geometrical height range as that from within the neighboring granule on the DC side. LoSs that pass through the dark lane are all located on the DC side of the sharp edge where the $\tau = 1$ surface drops into the MFC; however, they sense a distinctly lower temperature than in the surrounding areas further away, which makes them dark in *G*-band intensity. The low temperature comes about from enhanced radiative losses of the close surroundings into the MFC and the reduced temperature within the MFC compared to the surroundings at the same geometrical height. At the edge of the granule next to the dark lane on the limb side, the LoS intersects a larger portion of the flux tube where density, and with it opacity, is reduced compared to the unperturbed atmosphere (bottom-left panel of Figure 5). Consequently, the $\tau = 1$ surface forms at a deeper level at the granular walls,

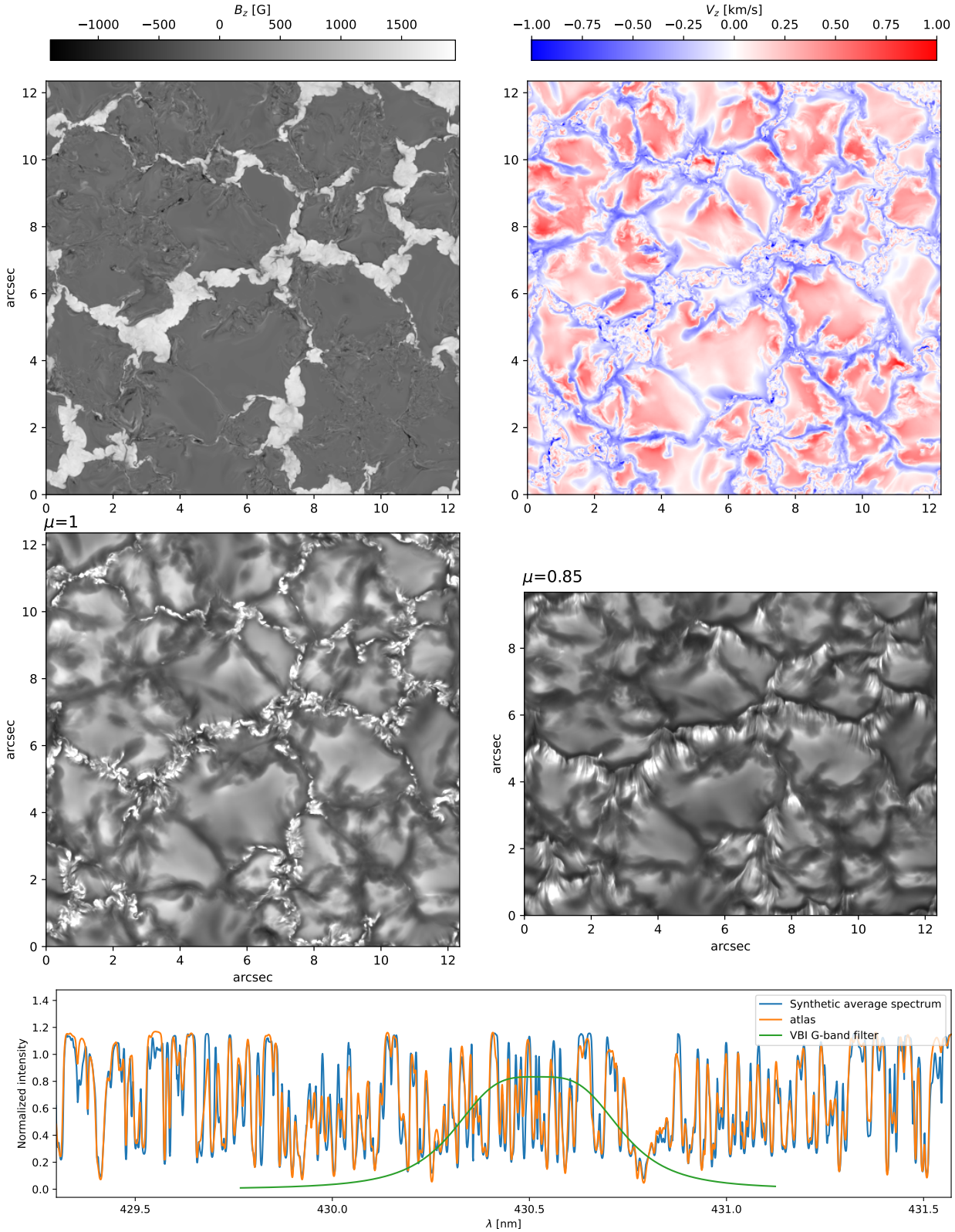

Figure 3. Overview of the MURaM simulation of a plage-like atmosphere. Top row: vertical magnetic flux density and vertical velocity at the horizontally averaged height where the optical depth $\tau_{500\ \mathrm{nm}}$ is unity. Middle row: synthetic *G*-band images at disk center ($\mu = 1$, left panel) and off disk center ($\mu = 0.85$, right panel) computed from the MURaM snapshot using the RH code. The limb direction is downward and the *y*-axis is foreshortened for the limbward image in the right panel. Bottom panel: synthetic *G*-band spectrum (blue line) at disk center averaged over the full FOV. The orange line represents the FTS atlas profile from H. Neckel & D. Labs (1984) for comparison, while the green line depicts the experimental transmission profile of the VBI *G*-band filter.

where the temperature is higher (∼7000 K) compared to the temperature within granular cells (∼6000 K), resulting in the appearance of bright faculae (top-left panel of Figure 5). The results are in agreement with the previous conclusions drawn from similar analyses (M. Carlsson et al. 2004; C. U. Keller et al. 2004; O. Steiner 2005).

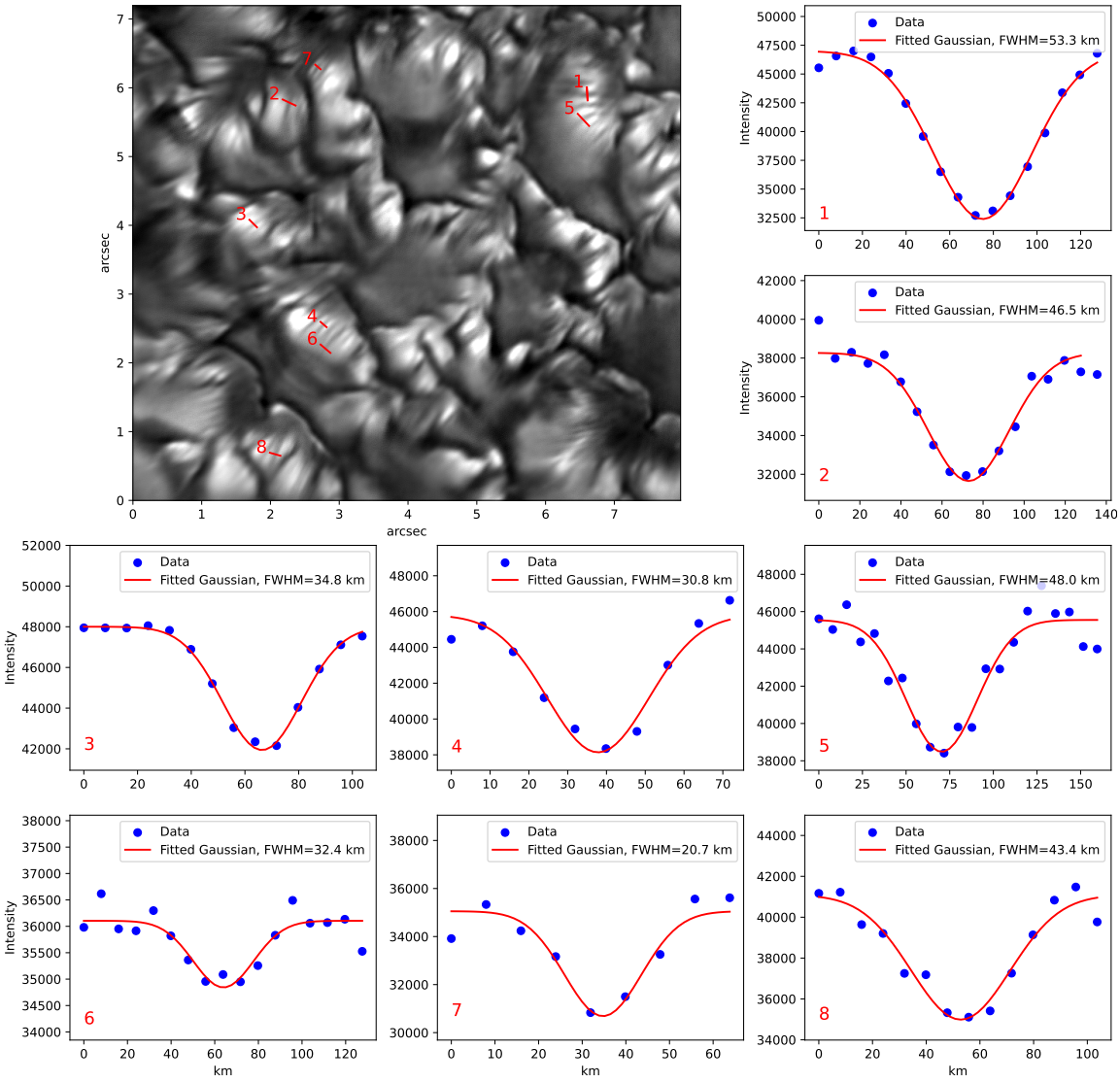

Figure 4. *G*-band intensity profiles along the crosscuts of dark/bright striae marked with red dashes in the top-left observed *G*-band image. Gaussian fits of the individual profiles are overplotted in red.

4.4. Striation

Similar to the observations, striation along faculae is also apparent in the synthetic *G*-band images from the simulation at $\mu = 0.85$ (top-left panel of Figure 5). To quantify their widths in the simulated images, we examine the FWHM of the Gaussian fits to intensity profiles along crosscuts of individual striae. Figure 6 displays the intensity profiles of eight randomly selected dark striae, with the corresponding Gaussian fits. The FWHM of these profiles ranges from 17 to 46 km, very similar to the FWHM from the observations given in Section 4.1. We note that the intensity cuts used for the FWHM calculations are taken mostly perpendicular to both the observed and synthetic striae (Figures 4 and 6). However, in some instances, due to local intensity variations, the cuts are slightly tilted from the perpendicular direction to avoid such local intensity variations for the Gaussian fit. Since the widths of the structures are very narrow (a few pixels), the slight tilt of the crosscuts does not affect the FWHM estimates.

The top panels of Figure 5 show that the dark striae coincide with elevated $\tau = 1$ heights. The difference in heights of the $\tau = 1$ surface between the narrow, dark features and their surrounding areas ranges for instances 1–8 of Figure 6 from 10 to 30 km.

Maps of Stokes parameters of the spectral line Fe I 630.2 nm, synthesized with the same MURaM datacube at $\mu = 0.85$, also reveal striations that are cospatial with those seen in the synthetic *G*-band images. The magnetic field at the formation height of Fe I 630.2 nm is predominantly vertical with respect to the surface, making the vertical component (B_z hereafter) the dominant one, while the *x*- and *y*-components can be neglected. For large heliocentric angles, Stokes *V* is determined by B_z and the viewing angle (i.e., the projection of B_z along the LoS). At $\mu = 0.85$, B_z also has a strong transversal component with respect to the observer. As a result, striations can also be seen in maps of Stokes *Q* or *U* (not shown here).

Figure 7 displays the *G*-band intensity, B_z (relative to the surface) at $z = 0$, and the Stokes-*V* signal along the dashes crossing the striations. It demonstrates that the *G*-band striation is closely correlated with variations in B_z and the Stokes-*V* signal in the sense that B_z is weaker in the dark striae than in the neighboring bright ones. Variation of B_z associated with the striation ranges from approximately 100 to 250 G (Figure 7).

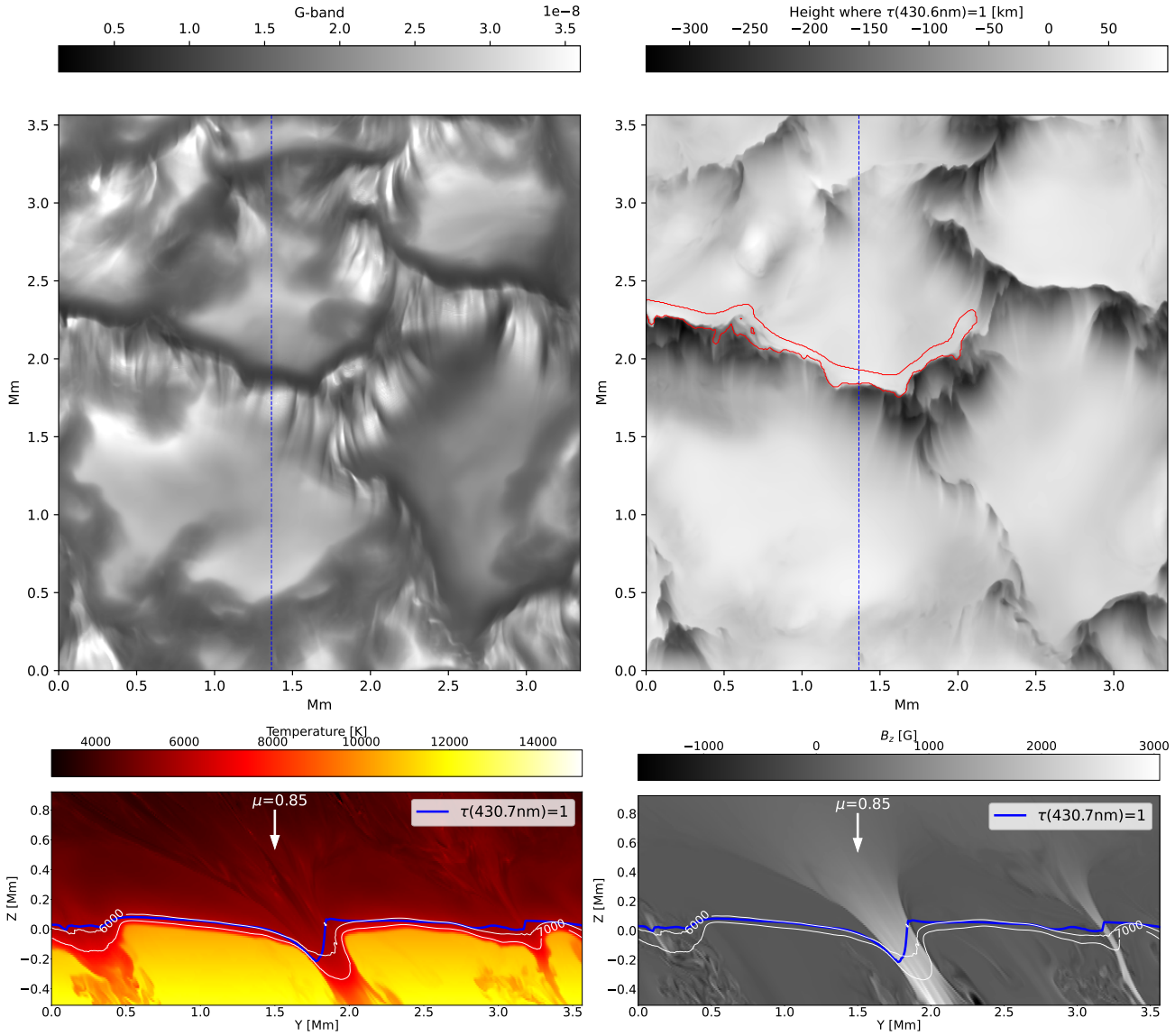

Figure 5. Top: synthetic *G*-band image of a simulation snapshot (left panel) and corresponding map of the height where the optical depth reaches unity in the *G*-band continuum at 430.7 nm. The red contour indicates the location of a dark lane starting at $x, y \approx (0, 2.4)$ in the *G*-band image. The limb is in the downward direction of the images. Bottom: vertical cuts through the temperature and LoS magnetic field strength along the blue dotted line marked in the top panels. Isothermal contours at $T = 6000$ and 7000 K are overplotted as white lines. Blue lines follow the $\tau = 1$ height.

5. Discussion and Conclusion

High-resolution *G*-band filtergrams obtained with DKIST, the largest solar optical telescope, reveal that facular regions exhibit a very thin and delicate striation pattern, consisting of dark and bright striae. The width of these narrow features ranges from approximately 20 to 50 km (Figure 4), indicating that they are either below the resolution limit of 1 m-class solar telescopes or appear with an overestimated width when resolved. Moreover, some of the detections are close to the spatial resolution of the analyzed DKIST data ($\sim 0\farcs03$), suggesting that the phenomenon most likely exists on even smaller spatial scales.

We successfully reproduced striated facular brightenings using a MURaM snapshot and radiative transfer calculations with spatial resolution and heliocentric angle comparable to the DKIST observations (Figure 3). The striations in the synthetic *G*-band images exhibit morphological characteristics, such as orientation, width, and length, similar to those of the observations (Figure 6). Similar to the observations, the width of some individual striae is around 17–20 km, which is close to the smallest possible scale in a simulation with 7 km grid spacing, meaning that these features could be even finer. Analysis of numerical simulations and synthetic images confirms that the striations seen in filtergrams are linked to spatial variations in photospheric magnetic flux density, which cause shifts in the geometrical height where the emergent continuum intensity forms—a phenomenon known as Wilson depression (Figures 5 and 7). Some fine-scale striations in the synthetic images arise from variations in the magnetic field as small as 100 G and showing a Wilson depression as small as 10 km (top panels of Figure 5).

The origin of the magnetic field variations remains an open question, which requires further investigation. A proposed mechanism for creating such variation is the flute instability (also called "interchange instability"), which could lead to a corrugated magnetic surface on flux tubes (M. Bünte 1993;

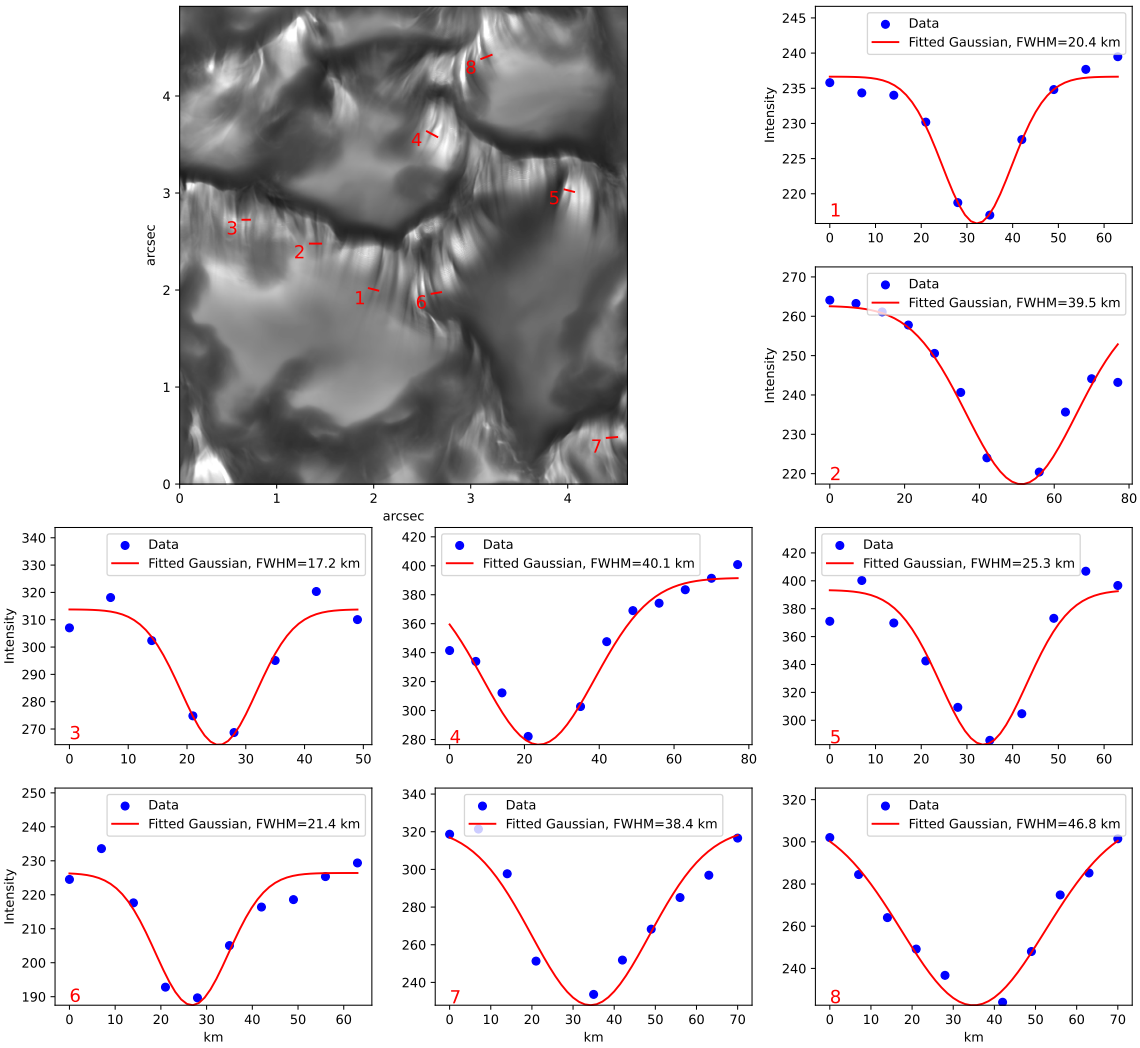

Figure 6. Synthetic *G*-band intensity profiles along the crosscuts of dark/bright striae marked with red dashes in the top-left simulated *G*-band image computed for $\mu = 0.85$. Gaussian fits of the individual profiles are overplotted in red.

H. C. Spruit et al. 2010; R. Schlichenmaier et al. 2016). This instability can develop from perturbations at the flux-tube boundary and can alter the tube's shape (surface structure). Theoretical studies suggest that magnetic flux tubes in the photosphere near $\tau_{500\,\mathrm{nm}} = 1$ can be unstable to the flute instability, leading to significant surface deformations (M. Bünte 1993; H. C. Spruit et al. 2010). Striations are also evident in Fe I 630.2 nm Stokes-*V* maps synthesized using the same MURaM datacube at $\mu = 0.85$. Moreover, there is a close correlation between Stokes-*V* and *G*-band signals along the dashes crossing the striations (Figure 7). They have similar widths and lengths in the synthetic Stokes-*V* maps as their *G*-band counterparts. Therefore, high spatial resolution is also necessary to resolve them in magnetograms and/or polarization maps. The excellent agreement between simulated and observed data suggests that DKIST *G*-band images trace variations of magnetic field strength and the footprints of Wilson depressions at similar scales. We note that the same plage region analyzed in this work has also been observed with the slit-based ViSP spectropolarimeter at DKIST, in the spectral channel that covers the magnetically sensitive photospheric lines Fe I 630.1/630.2 nm (see details in D. Kuridze et al. 2024). However, the resolution of the data ($\gtrsim$0.″2) was insufficient to resolve the striation in the magnetograms. Future DKIST spectropolarimetric observations with improved spatial resolution with ViSP, along with the upcoming Visible Tunable Filter, can target the magnetic striation.

Our analysis has also confirmed that facular brightenings are hot granular areas seen as a result of opacity reduction due to MFC of reduced mass density in front of them. The dark lanes form near the DC side edges of vertical MFCs viewed at an angle (Figure 5).

We would like to add that striations have also been detected in DKIST/VBI observations in the blue-continuum channel at 450 nm at a large heliocentric angle ($\mu = 0.85$) near NOAA Active Region 1282 (not shown). We synthesized blue-continuum images using MURaM snapshots and the RH code (not shown) at different heliocentric angles and found that the striation in this channel has very similar appearance and properties to that observed in the *G* band.

The presented work demonstrates that facular striation provides a unique opportunity to observe spatial variations in magnetic flux density of very small spatial scale and amplitude with unprecedented detail. The small spatial scales and high sensitivity to magnetic flux variations suggest that striation may evolve on extremely short dynamical timescales. Investigating their temporal evolution and dynamical

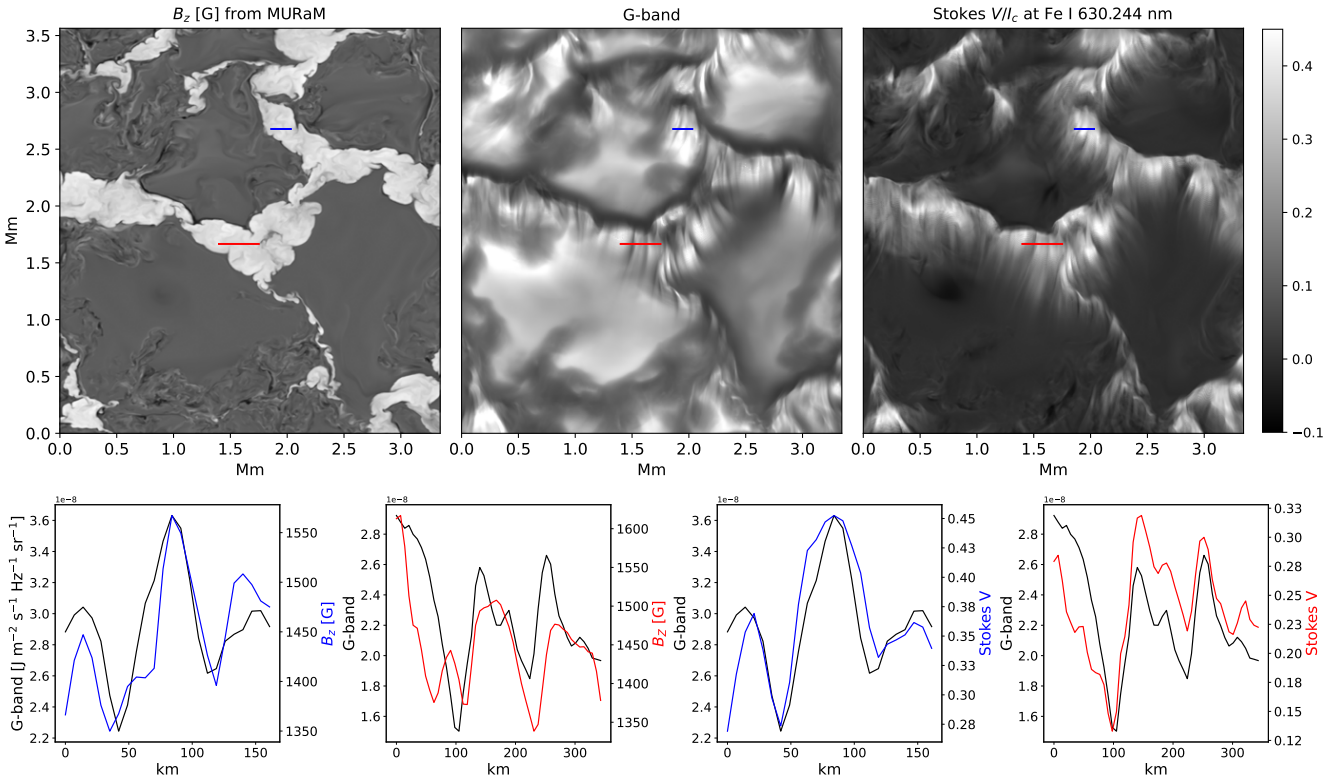

Figure 7. Top: maps of the vertical magnetic flux density, B_z, from the MURaM snapshot at the height $z = 0$ and Stokes-V amplitude (blue lob) of the spectral line Fe I 630.244 nm (right) normalized to the local continuum intensity. Bottom: G-band intensity, B_z, and Stokes-V profiles along the red and blue lines crossing the dark striae.

properties is beyond the scope of this Letter. However, we plan to explore this in a follow-up study, including flute instability as a potential formation mechanism, using high spatial and temporal resolution data and simulations. Additionally, we plan to synthesize G-band spectra and images from MURaM simulations with a grid spacing of 2−4 km to investigate whether striation appears at scales smaller than DKIST's spatial resolution limit.

We note that apart from faculae, striation is observed in other photospheric structures such as pores and sunspot light bridges (B. W. Lites et al. 2004). The fibrillar structure of the sunspot penumbra may have a similar origin as well. Therefore, similar high-resolution observational and modeling studies could be conducted to examine whether the findings presented in this work apply to other types of photospheric striations as well. Furthermore, magnetically induced striation is also observed in more remote astrophysical objects such as molecular clouds, i.e., the Polaris flare molecular cloud (R. Skalidis et al. 2023) or the Taurus molecular cloud (M. Heyer et al. 2016). Thus, we believe that the phenomenon is of general astrophysical interest and could even become the subject of laboratory experiments.

Acknowledgments

The research reported herein is based on data collected with DKIST, a facility of the National Science Foundation. DKIST is operated by the National Solar Observatory under a cooperative agreement with the Association of Universities for Research in Astronomy, Inc. DKIST is located on land of spiritual and cultural significance to Native Hawaiian people. The use of this important site to further scientific knowledge is done so with appreciation and respect. This material is based upon work supported by the NSF National Center for Atmospheric Research, which is a major facility sponsored by the US National Science Foundation under Cooperative Agreement No. 1852977. We would like to acknowledge high-performance computing support from the Derecho system (doi:10.5065/qx9a-pg09) provided by the NSF National Center for Atmospheric Research (NCAR), sponsored by the National Science Foundation. D.K. acknowledges the Georgian Shota Rustaveli National Science Foundation project FR-22-7506. D.K. acknowledges the Science and Technology Facilities Council (STFC) grant ST/W000865/.

ORCID iDs

David Kuridze https://orcid.org/0000-0003-2760-2311
Han Uitenbroek https://orcid.org/0000-0002-2554-1351
Matthias Rempel https://orcid.org/0000-0001-5850-3119
Alexandra Tritschler https://orcid.org/0000-0003-3147-8026
Oskar Steiner https://orcid.org/0000-0003-4708-1074

References

Asplund, M., Grevesse, N., Sauval, A. J., & Scott, P. 2009, ARA&A, 47, 481
Berger, T. E., Rouppe van der Voort, L., & Löfdahl, M. 2007, ApJ, 661, 1272
Berger, T. E., Rouppe van der Voort, L. H. M., Löfdahl, M. G., et al. 2004, A&A, 428, 613
Berger, T. E., Schrijver, C. J., Shine, R. A., et al. 1995, ApJ, 454, 531
Berger, T. E., & Title, A. M. 2001, ApJ, 553, 449
Bünte, M. 1993, A&A, 276, 236
Carlsson, M., Stein, R. F., Nordlund, Å., & Scharmer, G. B. 2004, ApJL, 610, L137
De Pontieu, B., Carlsson, M., Stein, R., et al. 2006, ApJ, 646, 1405

Heyer, M., Goldsmith, P. F., Yıldız, U. A., et al. 2016, MNRAS, 461, 3918
Hirzberger, J., & Wiehr, E. 2005, A&A, 438, 1059
Keller, C. U., Schüssler, M., Vögler, A., & Zakharov, V. 2004, ApJL, 607, L59
Kuridze, D., Uitenbroek, H., Wöger, F., et al. 2024, ApJ, 965, 15
Lites, B. W., Scharmer, G. B., Berger, T. E., & Title, A. M. 2004, SoPh, 221, 65
Neckel, H., & Labs, D. 1984, SoPh, 90, 205
Rempel, M. 2014, ApJ, 789, 132
Rempel, M. 2020, ApJ, 894, 140
Rimmele, T. R., Warner, M., Keil, S. L., et al. 2020, SoPh, 295, 172
Rutten, R. J., Kiselman, D., Rouppe van der Voort, L., & Plez, B. 2001, in ASP Conf. Ser. 236, Advanced Solar Polarimetry—Theory, Observation, and Instrumentation, ed. M. Sigwarth (San Francisco, CA: ASP), 445
Schlichenmaier, R., von der Lühe, O., Hoch, S., et al. 2016, A&A, 596, A7
Schüssler, M., Shelyag, S., Berdyugina, S., Vögler, A., & Solanki, S. K. 2003, ApJL, 597, L173
Skalidis, R., Gkimisi, K., Tassis, K., et al. 2023, A&A, 673, A76
Spruit, H. C. 1976, SoPh, 50, 269
Spruit, H. C., Scharmer, G. B., & Löfdahl, M. G. 2010, A&A, 521, A72
Steiner, O. 2005, A&A, 430, 691
Steiner, O., Hauschildt, P. H., & Bruls, J. 2001, A&A, 372, L13
Uitenbroek, H. 2001, ApJ, 557, 389
Wöger, F., Rimmele, T., Ferayorni, A., et al. 2021, SoPh, 296, 145
Wöger, F., von der Lühe, O., & Reardon, K. 2008, A&A, 488, 375
Yeo, K. L., Solanki, S. K., Krivova, N. A., et al. 2020, GeoRL, 47, e90243